

# Megavolt Bremsstrahlung Measurements from Linear Induction Accelerators Demonstrate Possible Use as a FLASH Radiotherapy Source to Reduce Acute Toxicity

Stephen Sampayan (✉ [sampayan1@llnl.gov](mailto:sampayan1@llnl.gov))

Lawrence Livermore National Laboratory

Kristin Sampayan

Opcondys, Inc. 600 Commerce Court

George Caporaso

Lawrence Livermore National Laboratory

Yu-Juan Chen

Lawrence Livermore National Laboratory

Steve Falabella

Lawrence Livermore National Laboratory

Steven A. Hawkins

Lawrence Livermore National Laboratory

Jason Hearn

University of Michigan

James Watson

Lawrence Livermore National Laboratory

Jan-Mark Zentler

Lawrence Livermore National Laboratory

---

## Research Article

**Keywords:** FLASH radiotherapy, linear induction accelerator, toxicity

**Posted Date:** April 28th, 2021

**DOI:** <https://doi.org/10.21203/rs.3.rs-472437/v1>

**License:**  This work is licensed under a Creative Commons Attribution 4.0 International License.

[Read Full License](#)

---

**Version of Record:** A version of this preprint was published at Scientific Reports on August 24th, 2021.  
See the published version at <https://doi.org/10.1038/s41598-021-95807-9>.

1  
2  
3  
4  
5  
6  
7  
8  
9  
10  
11  
12  
13  
14  
15  
16  
17  
18  
19

**Megavolt Bremsstrahlung Measurements from Linear Induction Accelerators Demonstrate Possible Use as a FLASH Radiotherapy Source to Reduce Acute Toxicity**

Stephen E. Sampayan<sup>a,b\*</sup>, Kristin C. Sampayan<sup>b</sup>, George J. Caporaso<sup>a</sup>,  
Yu-Jiuan Chen<sup>a</sup>, Steve Falabella<sup>a</sup>, Steven A. Hawkins<sup>a</sup>, Jason Hearn<sup>c</sup>,  
James A. Watson<sup>a</sup>, and Jan-Mark Zentler<sup>a</sup>

---

<sup>a</sup> Lawrence Livermore National Laboratory, P.O. Box 808, Livermore, CA 94551, USA  
<sup>\*</sup>Corresponding author e-mail address: sampayan1@llnl.gov  
<sup>b</sup> Opcondys, Inc. 600 Commerce Court, Manteca, CA 95336, USA  
<sup>c</sup> Department of Radiation Oncology, University of Michigan, Ann Arbor, MI 48109, USA

1  
2  
3  
4  
5  
6  
7  
8  
9  
10  
11  
12  
13  
14  
15  
16  
17  
18  
19

*Abstract*

Recent studies indicate better efficacy and healthy tissue sparing with high dose-rate FLASH radiotherapy (FLASH-RT) cancer treatment. This technique delivers a prompt high radiation dose rather than fractional doses over a longer period of time. The threshold is  $>40 \text{ Gy-s}^{-1}$  with a maximal effect at  $>100 \text{ Gy-s}^{-1}$  that must be maintained in the treatment volume. Mechanisms are still widely debated, but toxicity is minimized while inducing apoptosis in malignant tissue. Delivery technologies to date show that a capability gap exists with clinic scale, broad area, deep penetrating, high dose rate capability. Based on present trends, if FLASH-RT is adopted, it may become a dominant approach except in the least technologically advanced countries. The linear induction accelerator (LIA) developed for high current, high repetition rate, species independent charged particle acceleration, has yet to be considered for this application. We briefly review the status of LIA technology, explore the physics of bremsstrahlung-converter-target interactions and our work on stabilizing the electron beam. While the gradient of the LIA is low, we present our preliminary work to improve the gradient by an order of magnitude, presenting a point design for a multibeam FLASH-RT system using a single accelerator for application to conformal FLASH-RT.

**Introduction**

Recent studies indicate better efficacy with high dose-rate FLASH radiotherapy treatment (FLASH-RT). This technique delivers a prompt high radiation dose, sometimes in a single treatment rather than spacing the dose over a longer period of time [ 1 2 3]. While the

1 healthy tissue sparing effect associated with FLASH-RT has a threshold of  $40 \text{ Gy}\cdot\text{s}^{-1}$ , a maximal  
2 effect occurs at  $>100 \text{ Gy}\cdot\text{s}^{-1}$ , with some techniques using instantaneous dose rates as high as  
3  $10^8 \text{ Gy}\cdot\text{s}^{-1}$  in a single 23-MeV, 1 ns, proton pulse [ 4 5 6 7]. Hypothesized mechanisms include  
4 oxygen depletion or a modified immune response.

5 Human trials are still very limited with one report of  $167 \text{ Gy}\cdot\text{s}^{-1}$  (15-Gy in 90-ms)  
6 delivered for treatment of a 3.5-cm diameter skin tumor (Fig. 1). This treatment used electrons  
7 from an Oriatron eRT6 5.6 MeV microwave LINAC at the Lausanne University Hospital [ 8 9].  
8 Although it was not possible to draw any firm conclusions, the trial demonstrated treatment  
9 was feasible and safe and showed a favorable outcome for normal skin. Tumor response  
10 appeared rapid and complete.

11 Pulsed power accelerators store energy over a comparatively long time and are  
12 discharged in 10s to 100s of nanoseconds to deliver pulsed high-power beams. While  
13 anecdotal, one of the authors is aware of three separate accounts of the same accidental FLASH  
14 dose event that occurred in the mid-1960s. A single pulse, 7-8 MeV, 50 ns pulsed power FLASH  
15 electron accelerator accidentally fired while an individual was in the radiation vault. At least  
16 one account purports the individual observed a “blue flash” consistent with the recent single  
17 human trial [ 8]. The individual received near the  $\text{LD}_{50}$  bremsstrahlung dose with little, if any,  
18 clinical effect [ 10]. Soon afterwards, this same type of pulsed power accelerator was used in  
19 some of the original FLASH radiation effect studies on mammalian tissue. That research served  
20 as the basis for the work today[ 11].

1           Although some believe FLASH-RT holds great promise and is perhaps the biggest  
2 development in recent radiotherapy history, some remain skeptical about the replication of  
3 efficacy and have concerns about technical complexity, the lack of understanding of its  
4 molecular radiobiological underpinnings, and reliability [ 12]. Clearly, significant work remains  
5 to be done.

6           A survey of FLASH-RT delivery systems is shown in Figure 2 with added details provided  
7 in Table I. We clearly show the need for clinic scale multi-MV FLASH-RT systems. Here we plot  
8 the dose rate as a function of range (in terms of  $R=\rho dx$ ) for electrons, photons, and protons [ 3  
9 7 9 13 14 15 16 17 18 19 20 21 22 23 24]. We make a distinction between clinic scale systems  
10 that would fit in a nominal treatment vault of about 100 m<sup>3</sup> (solid blue filled markers) from  
11 more costly research centers as well as specialized high energy proton facilities (open markers).  
12 Each of these facilities provides a nominal FLASH-RT area ranging from 7.5x10<sup>-5</sup> cm<sup>2</sup> at a range  
13 of about 1.3 gm-cm<sup>-2</sup> for 20 MeV protons to the largest area of 55 cm<sup>2</sup> at a range of about 3 gm-  
14 cm<sup>-2</sup> for 6 MeV electrons. Energetic proton treatment areas ranged from 0.8-3 cm<sup>2</sup>  
15 corresponding to a range of 30-40 gm-cm<sup>-2</sup> for 230 MeV and above.

16           At least one critical review focused on non-differential tissue sparing results between  
17 FLASH-RT and conventional radiotherapy (CONV-RT) experiments [ 6]. In a specific study, mice  
18 were irradiated with microbeam radiation therapy (MRT) using a synchrotron 95 keV source [  
19 25]. The MRT beam was made up of quasi-parallel micro-planar beams with a width of 25 to  
20 100 μm that were typically spaced from 100 to 400 μm (i.e., valleys). Dose rates in the beams  
21 were between 276 to 319 Gy-s<sup>-1</sup>; scatter resulted in an order of magnitude lower dose rate

1 (presumed to be  $\approx 30 \text{ Gy}\cdot\text{s}^{-1}$ ) and total dose in the valleys. Toxicity post irradiation was  
2 quantified by the  $\text{TD}_{50}$  metric based on >15–20% weight loss, severe diarrhea, and moribund  
3 behavior. What was striking about the conclusion was that the MRT FLASH valley total dose  
4 (between 3.8-7.2 Gy at  $\text{TD}_{50}$  depending on irradiation site) was a better predictor of acute  
5 toxicity, having roughly the same effects as total dose using conventional ( $0.05\text{-}0.06 \text{ Gy}\cdot\text{s}^{-1}$  at 93  
6 keV) and synchrotron ( $37\text{-}41 \text{ Gy}\cdot\text{s}^{-1}$  at 124 keV) delivery. Further, the total dose for  $\text{TD}_{50}$  at the  
7 highest delivery rates increased as the treatment volume was reduced and were between 116-  
8 261 Gy greater. These results suggest that for FLASH-RT to be healthy tissue sparing, both the  
9 periphery and exit edge of the radiation needs to be above the threshold required for the  
10 effect; toxicity can be induced by low FLASH-RT dose rates. Further it also suggests that the  
11 volume of low dose rate should be minimized.

12 To increase the treatment area, beam scanning has been proposed. But we were unable  
13 to clearly delineate between collimated and hard-edge beams so as to minimize the delivery  
14 volume of below the FLASH-RT threshold. For a typical gaussian shaped beam resulting from a  
15 non-zero emittance, the dose rate is significantly lower at the beam edges which may result in a  
16 reduced tissue sparing FLASH effect [ 6 25]. Thus, it is not clear if there are biological  
17 consequences of irradiating with FLASH contributions below 100% as the approach has only  
18 started to be explored; it is unknown how this approach will influence the overall effect [ 26].

19 At present, clinic scale machines for FLASH-RT are limited to shallow tumors while deep  
20 seated tumors require the use of highly specialized and costly proton systems. Because of the  
21 energy deposition profile resulting from the Bragg peak, protons have the advantage of being

1 more conformal to the tumor volume. But as of 2017, only 1% of the world cancer patients are  
2 treated with protons or heavy particles. And even though the modality was introduced in 1954  
3 by Lawrence Berkeley National Laboratory, the primary limitation continues to be system cost  
4 (\$30-100M US) [ 27].

5           However, improvements in photon delivery have advanced. While intensity modulated  
6 spot scanning (IMPT-SS) using protons yields the most conformal external beam radiotherapy  
7 plans, photon therapy can be administered conformally if sufficient granularity is used. Previous  
8 studies using a pencil beam of photons with as few as three lines of sight yielded a 4% dose  
9 error over an idealized volume [ 28]. Helical tomotherapy (IMXT-HT) using fifty-one separate  
10 angles over 360° with sixty-four binary controlled beamlets and delivered in a helix pattern was  
11 comparable to other forms of proton therapy such as distal gradient tracking (IMPT-DGT) [ 29].

12           Large treatment areas ( $\approx 350 \text{ cm}^2$  @1 m as we will demonstrate here) and long range  
13 ( $\approx 25 \text{ gm-cm}^{-2}$ ) can be achieved with megavolt (MV) photons. Utilizing multi lines of sight for  
14 near conformal therapy, they can be an alternative to fill the void between shallow treatment  
15 with microwave linacs and deeper treatment with expensive proton therapy systems [ 6]. While  
16 many of the clinic scale FLASH-RT systems can be converted to MV photons, beam loading and  
17 fundamental beam stability limitations sets practical limits to below ampere level beams and  
18 low dose rates for single accelerator systems [ 30].

19           Clinic scale microwave accelerators rely on the longitudinal resonance of a sinusoidally  
20 varying electromagnetic field in parallel with the electron motion; electrons in resonance  
21 experience a net positive accelerating gradient (i.e., the energy gained by a charge particle per

1 length of accelerator) [ 31]. To increase dose rates requires higher current. Higher currents,  
2 however, affect the electromagnetic wave resonance with the electron longitudinal motion and  
3 can result in a lower gradient [ 32 33]. In one example, an increase from 0.3-A peak current to  
4 1.2-A peak current reduced the exit gradient from 12.7-MV-m<sup>-1</sup> to 2.5-MV-m<sup>-1</sup> resulting in lower  
5 output energy [ 34]. Further, the beam break-up instability, which induces uncontrolled  
6 transverse beam motion that causes the beam to be lost to the walls, scales as the square-root  
7 of the beam current divided by the radius of the cavity [ 35 36]. This effect can shorten the  
8 beam pulse at higher currents.

9 An alternate acceleration technology, the linear induction accelerator (LIA), is based on  
10 a pulsed power approach and is mature [ 37]. It was developed in the 1960's to overcome the  
11 beam current limitations in microwave linear accelerators. The systems are inherently FLASH,  
12 high dose rate systems. When converted to bremsstrahlung, systems have demonstrated the  
13 equivalent dose rates well in excess of the 100 Gy-s<sup>-1</sup> upper threshold.

14 The concept relies on magnetic induction (Fig. 3). A magnetic core surrounds an  
15 evacuated accelerator tube where each core is enclosed within a conductive cavity. When a  
16 pulse is applied to a winding around the core, a longitudinal electric field is generated. By  
17 referencing one side of the pulsed source to the cavity interior, the electric field is net  
18 accelerating as  $\oint E \cdot dl = 0$  everywhere except in line segment *BC* (Fig. 3). This electric field is  
19 maintained for the pulse duration so long as the magnetic core does not saturate (i.e., the point  
20 at which leakage current around the core increases and the electric field collapses). This  
21 saturation effect is based on the core material, the cross-sectional area, and the volt-second

1 product of the applied pulse [ 38]. To return the core back to the original magnetic state after  
2 the acceleration pulse, a small voltage opposite to the applied pulse is maintained across each  
3 cavity.

4 The LIA is charge to mass ratio independent, only requiring that the pulsed sources be  
5 synchronized, and the beam dynamics be properly managed. Experiments have demonstrated  
6 high dose-rate ion beams (2 A of He<sup>+</sup>, 2.4 ns pulse, and a 1 mm radius spot) using accelerator  
7 cavities originally designed for electrons [ 39 40]. Because the beam pipe radius can be  
8 arbitrary, accelerating multiple beamlets through a single accelerator cavity enables  
9 acceleration of multiple beams through a single accelerator [ 41 42]. Such an approach greatly  
10 simplifies a conformal FLASH-RT system. Since the beam pipe radius can be arbitrary,  
11 suppression of beam instabilities is straightforward as the effect scales as the current divided by  
12 the beam pipe radius squared [ 36].

13 To illustrate the extensive use of LIA technology, we list noteworthy systems with  
14 energy >5-MeV in Table II [ 38 42 43 44 45 46 47 48 49 50 51 52 53 54]. These machines serve  
15 as the basis for numerous other uses that include intense charged particle beam propagation,  
16 free electron laser, dynamic FLASH radiography for weapons research, fusion experiments, and  
17 pulsed radiation effects studies.

18 The LIA is a very simple and robust device and of relatively low cost. Because resonance  
19 is not required to accelerate the charge particles, temperature fluctuations have a minor effect  
20 on operation. While large and expensive accelerators are being proposed for investigating  
21 FLASH-RT, developments in LIAs in recent years for other applications offer a wide range of

1 compact and less expensive approaches that could be optimized for specific FLASH applications  
2 when they are established; some of these developments will be illustrated here [ 1]. Here we  
3 present an alternative accelerator technology for use in FLASH-RT.

4

## 5 **Results**

6 Photons generated by an LIA potentially provide broad area, deep penetrating, and high  
7 dose rate capability. To date, no MV broad beam photon sources have been characterized  
8 sufficiently to determine relevance to FLASH-RT. Here, we present experiments and  
9 measurements on the FLASH X-ray (FXR) accelerator used to accelerate electrons to 17 MeV  
10 and also on the Experimental Test Accelerator-II (ETA-II) with a nominal output energy of 6.5  
11 MeV, but high repetition rate.

12 FXR is an active research facility mainly used for hydrodynamic experiments [ 55].  
13 Conversion to bremsstrahlung is with a Ta target. The beam is approximately 70 ns FWHM long  
14 with a focal spot that is nominally  $\approx 1.5$  mm to ensure high resolution imaging. For MV photon  
15 FLASH-RT to be viable using any pulse format, the focus of the beam must be stable pulse to  
16 pulse. It is well known that even in ultra-high vacuum monolayer formation on the target is  
17 rapid and scales in seconds as  $\frac{3.2 \times 10^{-6}}{P}$ , where P is the pressure in mbar. Once the beam  
18 impacts the surface, this monolayer, as well as gas impurities present even in highly purified  
19 metals, is released, and forms a plasma. Because the electron beam provides a strong negative  
20 potential, ions are extracted from the plasma boundary into the beam (Fig. 4a and 4b). The  
21 result is a dynamically varying focus on a prompt time scale.

1            In Figure 4c, using a load lock transfer procedure, we performed analysis of the Ta  
2    bremsstrahlung converter targets operated at  $10^{-7}$  to  $10^{-8}$  T in the accelerator. Prior to analysis,  
3    an Au overcoating was used to confine and prevent contaminant introduction into the  
4    measurements. With Rutherford backscattering (RBS) at 2 MeV  $\text{He}^+$ , forward Rutherford  
5    scattering (FRS), and secondary ion mass spectrometry (SIMS), we assayed the contamination  
6    as  $\text{H}_2$  @  $1.5 \times 10^{15} \text{ cm}^{-2}$  and C @  $3 \times 10^{15} \text{ cm}^{-2}$  on the surface with 6 ppm  $\text{H}_2$  in the Ta matrix.

7            To determine the density of the contaminant ions created during the beam pulse, we  
8    implemented high aspect ratio Faraday cups at various distances from the target (Fig. 4d). This  
9    high aspect ratio was used to ensure measurement errors due to secondaries generated from  
10   the ion impact were minimal. A negative bias ( $\approx -50$  V) stripped the low energy plasma electrons  
11   from the measurement. For a Faraday cup stand-off distance of 25 cm, we observed negative  
12   scattered electrons during the beam pulse and fast ions approximately 90 ns after the beam  
13   first impacts the target. It appeared that this fast ion pulse begins as the electron beam  
14   terminates. On the slow time scale, we observe two components: one at 50  $\mu\text{s}$  and another at  
15   80  $\mu\text{s}$ . Each of these components correspond to an apparent speed of approximately 280  $\text{cm}\cdot\mu\text{s}^{-1}$ ,  
16   0.50  $\text{cm}\cdot\mu\text{s}^{-1}$ , and 0.31  $\text{cm}\cdot\mu\text{s}^{-1}$ , respectively which is in reasonable agreement with our  
17   hydrodynamic models [ 56]. From these signatures and the Faraday cup distance, we estimate  
18   the initial plasma density  $>10^{17} \text{ cm}^{-3}$  but falling off rapidly to approximately  $<10^{12} \text{ cm}^{-3}$  at about  
19   500 ns.

20            While the plasma is too slow to immediately impact the FLASH beam, the ions are not.  
21   To determine the impact of the ions on the bremsstrahlung spot size, we used a multi-frame x-

1 ray pinhole camera (see Methods section). The gate times were evenly spaced within the  
2 bremsstrahlung main FLASH pulse. What is clear from the first column of images (Fig. 4e) is a  
3 degradation of the focus in later frames. This effect manifests itself as a decreasing dose rate in  
4 time (Fig. 4f – marked “unstable focus”). This effect is far too fast to correct electronically (i.e.,  
5 readjusting the focusing magnetic field). However, by using the pinhole camera for beam  
6 characterization and under focusing the beam (i.e., focused minimum beyond the target) we  
7 were able to achieve a net uniform spot and constant dose rate (Fig 4f – marked “stable  
8 focus”). Typical optimized spot size was approximately 1.5 mm FWHM.

9           With an optimized focus, we performed total dose measurements during the 70 ns  
10 pulse to determine the collimated flat field and the shot-to-shot repeatability. The geometry for  
11 the measurement is shown in Figure 4g. This particular measurement consisted of the  
12 bremsstrahlung converter target, a fast CVD diamond FLASH dose detector, an 8 cm thick low  
13 energy filter, and either thermoluminescent (TLD) or film detector at 1-2 m [ 57]. The CVD  
14 diamond FLASH detector is range thin to the photons so as not to perturb the measurement.  
15 Figure 4h shows a flat field for 90-100% as approximately 21 cm diameter at 1 m. This  
16 measurement corresponds to approximately a 350 cm<sup>2</sup> area. We measured a 6° half angle  
17 through the collimator at 17 MeV electron energy. The cone angle was a result of the  
18 combination of the off normal electron trajectories and beam energy; the latter contribution  
19 scales as  $\frac{1}{\gamma}$  where  $\gamma = 1 + \frac{E_{beam}}{m_0c^2}$ , ( $E_{beam}$  – incident beam energy,  $m_0c^2$  – energy of an electron at  
20 rest or 0.511 MeV).

1 To measure the pulse-to-pulse repeatability, we used the CVD diamond flash detector  
2 immediately after the target. This detector provides a fast signal that is recorded. For  
3 calibration we used an array of thermoluminescent dosimeters (TLDs). Bremsstrahlung was not  
4 generated on all pulses. In Figure 4i, we measured the calibrated dose level and variation shot  
5 to shot. In that measurement, we observe approximately 4.19 Gy total integrated dose in the  
6 70 ns pulse with a variation of approximately  $1\sigma \approx 0.16$  corresponding to a 3.9% variation. This  
7 value corresponds to an instantaneous dose rate of approximately  $6 \times 10^7 \text{ Gy-s}^{-1}$ .

8 The experimental test accelerator (ETA-II) is a high repetition rate system reconfigurable  
9 for accelerator development. It was designed to deliver highly stable electron beams with less  
10 than 1% energy variation, millimeter spot size, and submillimeter spot motion at 5,000 Hz (Fig.  
11 5a, upper). Initial use of the accelerator was in conjunction with a wiggler to generate  
12 electromagnetic energy similar to ESRF and IMBL (Table I), but delivered 2 GW at 140 GHz mm-  
13 wave energy for fusion research studies [ 16 17 58]. Because of the pulse width requirement  
14 that was based on an older design, the machine gradient was only  $<0.5 \text{ MV-m}^{-1}$ .

15 Here, we explore repetition rate operation of an LIA. The pulsed source for ETA-II  
16 utilized thyatrons (Fig 5a, large cabinets) driving a Melville line (large vertical cylindrical  
17 structure to the left) [ 59]. The overall schematic is shown in Figure 5b. A capacitor is charged  
18 and switched into the non-linear Melville transmission line. This pulse is sent through a step-up  
19 transformer and series saturable inductors that successively compress the energy in time to  
20 provide high peak power for each LIA core. At full voltage operation, the pulsed sources deliver  
21 135-kV into a 2-ohm load at 5,000-Hz at better than 90% efficiency. Four pulsed sources were

1 used to drive the accelerator; three drive sixty accelerator cavities and one drives the injector  
2 to deliver nominally  $\approx 3,000$ -A electron beam at 6.5-MeV in a 70-ns pulse.

3 Stability of the system (pulse-to-pulse variation and output energy) is determined by the  
4 state of the magnetic cores both in the accelerator and also in the pulsed sources. Excessive  
5 internal reflected energy improperly returned the magnetics to a varying state (i.e., reset). We  
6 observed the system to exhibit bipolar state behavior with large variations in timing. The upper  
7 plot (Fig 5c) shows a multipulse burst from the pulsed source at 5,000 Hz where the z axis is  
8 pulse number. The timing variations in this data set were so large that five pulses of the burst  
9 were outside the 2000 ns capture window. The data summary plot for timing (middle frame)  
10 and pulse-to-pulse energy regulation (lower frame) are also shown in the figure. While the  
11 timing variation was large, the pulse-to-pulse regulation was  $1\sigma < 1\%$ . To achieve lower jitter, we  
12 reduced reflected energy by better matching of the Melville line to the accelerator and also  
13 used more aggressive damping in the core reset system. The final result is shown in Figure 5d.  
14 Although a slight timing variation was seen for the first two pulses, the remaining pulses  
15 showed a timing variation of  $< 5$  ns while showing a pulse-to-pulse energy regulation of  $\approx 0.5\%$ .  
16 This result was confirmed with a magnetic energy analyzer at the end of the accelerator. If  
17 converted to bremsstrahlung, the net dose rate variation would be  $\pm 0.71\%$ .

18 We are presently designing and testing accelerator cavities with a goal to achieve higher  
19 acceleration gradients. The experimental arrangement is shown in Figure 5e. These particular  
20 cavities were initially insulated with SF6 pressurized gas which limited breakdown performance.  
21 At this stage of testing, we were able to achieve 0.210 MV across 0.165 m (Fig. 5f) or  $\approx 1.3$  MV-

1  $\text{m}^{-1}$  for a pulse width of 40 ns FWHM. This gradient is approximately 2-3 times the gradient of  
2 ETA-II and with oil insulation, we expect to achieve another doubling of that gradient.

3 To replace the existing pulsed source, we are testing high repetition rate, single crystal,  
4 semi-insulating SiC photoswitches driven by pulsed laser diodes (Fig. 5g-5h) [ 60]. We have also  
5 tested and utilized a configuration that charges capacitors in parallel and selectively discharges  
6 them in series to allow output voltage variability, and hence variable control of the electron  
7 final energy over a wide range [ 61]. Figure 5g shows a device under test in a low inductance  
8 geometry. In this particular geometry, the SiC (upper left inset) was integrated into a polyimide  
9 epoxy structure. This particular structure has been tested to approximately 30 kV under oil.  
10 Contacts were evaporated gold. The diode laser and driver are shown in the larger photo; the  
11 surface mount laser diode is shown in the upper right inset. Scale is 1 mm spacings. This  
12 particular diode was rated for 70 W pulsed output in the IR spectrum with a 0.1% duty cycle.  
13 Figure 5h shows the output at 1 MHz pulse repetition frequency. Risetime was approximately  
14 12 ns and was limited by the diode driver circuit.

15

## 16 **Discussion**

17 The MRT results using a synchrotron at 95 keV suggests that both the periphery and exit  
18 dose rate need to be above the healthy tissue sparing threshold to minimize toxicity [ 25].  
19 Based on this conclusion, we developed an approach for a FLASH-RT system using an LIA (Fig. 6)  
20 by first calculating the dose rate distribution for two cases. The first case was a single source at  
21  $100 \text{ Gy}\cdot\text{s}^{-1}$  at 1 m (Fig. 6a). The second case was four separate sources placed symmetrically

1 around the volume, each at  $25 \text{ Gy-s}^{-1}$  at 1 m (Fig. 6b) or  $100 \text{ Gy-s}^{-1}$  total. Each case relied on  
2 percent depth dose (PDD) experimental curves [ 62 63]. For simplicity, we used an idealized  
3 cylindrical volume with the mean value of the human abdominal circumference of  $\approx 1 \text{ m}$  or  
4 radius of  $\approx 16 \text{ cm}$  [ 64]. Source surface distance (SSD) was 1 m for all sources. Electron energy  
5 was 16 MeV. Conversion to bremsstrahlung was based on a Ta target.

6 In Figure 6a, while a healthy tissue sparing dose rate  $>40 \text{ Gy-s}^{-1}$  is delivered nearest the  
7 source, about 25% of the volume is below that dose rate. In Figure 6b, a symmetric  
8 configuration of four sources achieved 50% beyond the required healthy tissue sparing dose  
9 rate, or about  $60 \text{ Gy-s}^{-1}$  throughout the majority of the volume. The minimum dose rate in that  
10 volume decreases slightly to about  $56 \text{ Gy-s}^{-1}$  in the center of the volume. While dose build up  
11 was considered using the deposition curves, dose rate at the volume edge increased rapidly to  
12  $40 \text{ Gy-s}^{-1}$  in 1-2 cm because of the added contribution from the other sources. This result  
13 suggests that for MV bremsstrahlung FLASH-RT, multibeam delivery is necessary to remain  
14 above the healthy tissue sparing threshold. Thus, we baseline our approach using four sources,  
15 but to minimize the possibility of loss of a source, resulting in below the healthy tissue sparing  
16 dose rate, we rely on a single accelerator generating all of the separate beamlets.

17 We have demonstrated conversion of the electron beam to bremsstrahlung using Ta on  
18 both FXR and ETA-II and presented measurements of the physical processes of the beam-target  
19 interaction to produce a predictable through collimator dose. The measurement showed a  
20 uniform field of  $\approx 350 \text{ cm}^2$  at 1 m with a dose  $\approx 4.2 \text{ Gy}$  per pulse integrated over 70 ns.  
21 Instantaneous dose rate was  $\approx 6 \times 10^7 \text{ Gy-s}^{-1}$ . The pulse-to-pulse variation was  $1\sigma \approx 0.16$  or a

1 3.9%. This result is in contrast with the largest FLASH-RT field to date of a 55 cm<sup>2</sup> field using  
2 electrons [ 9].

3 On ETA-II, we demonstrated stable operation at 5 kHz both in timing (<5 ns) and energy  
4 variation delivered by the pulsed source (<0.5%).

5 Using photonic switches, we demonstrated 1 MHz repetition rates. Using the  
6 controllability of the device, the pulsed sources can be simplified to provide electron energy  
7 variability.

8 Here we use a 1.5 mm spot diameter and four separate beamlets to approximate  
9 conformal therapy; added beamlets reduce the bremsstrahlung converter requirement for a  
10 given dose rate. For scaling, we use the well-known relationship of electrons to bremsstrahlung  
11 dose rate as:  $1.7 \times 10^4 IV^{2.65}$  (in Gy-s<sup>-1</sup> for Ta at 1 m distance), where  $V$  is in MV and beam  
12 current  $I$ , is in kA.

13 The pulsed beams delivered for our ETA-II measurement had an instantaneous power  
14 density on the Ta target  $\approx 10^{12} - 10^{13}$  W-cm<sup>-3</sup>. At these power densities, the target undergoes  
15 rapid hydrodynamic expansion on the microsecond time scale and is therefore single use.  
16 FLASH-RT requires a minimum average dose-rate of only 40 to 100 Gy-s<sup>-1</sup> while maintaining the  
17 instantaneous dose rate  $10^1$ - $10^2$  times lower or  $\approx 10^6$  Gy-s<sup>-1</sup> [ 6]. These lower rates allow using  
18 electron beam repetition rate as a free parameter for the target approach.

19 Short duty cycle ( $\approx 30$  s) DC x-ray tubes using thermal inertia have achieved almost 200  
20 kW-cm<sup>-2</sup> [ 65]. 25 Gy-s<sup>-1</sup> total requires a 6.25 A beam at a 10 kHz rate with 15 ns pulses on each

1 of the converter targets (Methods section). For a 1.5 mm spot size, the instantaneous power  
2 flux is 850 kW-cm<sup>-2</sup> which is still clearly outside the range of present state-of the-art.

3 Two target approaches are still possible: Heat generated from a 1.5 mm electron spot  
4 size at 16 MeV and 6.25 A can be dissipated by rotating the target at an equivalent linear speed  
5 of 15 m-s<sup>-1</sup>. For an 8 cm radius disk, approximately 6 rotations are required for an 0.2 s  
6 treatment cycle of 20 Gy. Net local temperature rise is 725° C and well within the Ta melting  
7 temperature of 3017° C. For simplification, as a second approach, we modeled a liquid cooled  
8 multilayer target where each layer is designed to absorb ≈4% of the electron beam energy  
9 (total of 25 layers) [ 66]. In this model, each layer is allowed to convect heat away into a moving  
10 fluid (Fig 6c-6d). For the fluid, we assumed a convective heat transfer coefficient of 100 W-m<sup>-2</sup>-  
11 °K<sup>-1</sup>, a flow rate of 4.2 cm-s<sup>-1</sup> and allowed a 50° C temperature rise. Peak equilibrium  
12 temperature is approximately 110° C.

13 The high gradient LIA cavity concept is shown in Figure 6e, where the gradient is given  
14 by:  $\alpha \partial B \frac{R_o - R_i}{\tau}$ , where  $\alpha$  is the packing efficiency,  $\partial B$  is the flux swing of the cores,  $R_o$  and  $R_i$  are  
15 the magnetic core outer and inner diameters, respectively, and  $\tau$  is pulse width [ 67]. To provide  
16 the insulator interface between the magnetic core and vacuum region for the electron beam,  
17 we use multilayer insulators. These structures are made up of periodic layers of conductive and  
18 insulating material laminated into a monolithic structure. The structure provides an increase in  
19 breakdown electric field of up to 4x, is insensitive to polarity effects, photon and charge particle  
20 flux, and suppresses beam breakup instability resonances [ 68 69 70 71].

1 To allow enough room for multiple beams while keeping the cavity small to avoid  
2 unwanted beam breakup modes, we select a ferrite inner radius of  $R_i = 0.1\text{-m}$ . We also take,  $\partial B$   
3  $\approx 0.6\text{T}$  (NiZn ferrite), and  $\alpha = 60\%$  because of the insulator configuration [ 38]. The surface for  
4 the optimization trading  $\tau$  and  $R_i$  to achieve a given gradient is shown in Figure 6f. We show a  
5 design point of  $5\text{ MV/m}$  at a  $15\text{ ns}$  pulse width for  $R_o \approx 0.3\text{ m}$ .

6 A single LIA is used to accelerate separate beamlets in an approximately  $14\text{ cm}$  diameter  
7 beam pipe. While four beams are shown, eight can be easily implemented. Beam transport is  
8 managed through the accelerator with solenoid coils and integrated steering similar to FXR [  
9 55]. The added steering capability enables generating of oblique rays to allow a closer  
10 approximation of multibeam conformal therapy. At  $16\text{ MeV}$ , the system would be  
11 approximately  $3.2\text{ m}$  long (Fig. 6g) delivering an average dose rate of  $60\text{ Gy-s}^{-1}$  through an  
12 idealized  $16\text{ cm}$  radius volume.

13

## 14 **Methods**

15 We developed Figure 2 and Table I by performing an exhaustive search of FLASH-RT  
16 systems in the open literature leveraging the work of Esplen, Wilson, and Darafsheh [ 6 7 22]. In  
17 an attempt to standardize our methodology, we used spot size, range at energy, and average  
18 beam current to determine dose rates. For electron range, we used stopping power data from  
19 M.O. El-Ghossain over four tissue types [ 72]. For bremsstrahlung photons, we used the PDD  
20 data by Hill for low energy and those by Narayanasamy and Feye for MV energy [ 62 63 73]. The  
21 intense photon sources at ESRF and IMBL use wigglers. The spectra provided were

1 bremsstrahlung-like to first order and sufficient for this parameter survey; no added corrections  
2 were made. Turner provided the correction between a water phantom and tissue; again, no  
3 changes were necessary for our estimates [ 74].

4 For our dose-rate calculations, we used one range depth (i.e.,  $l/l_0 \approx e^{-1}$ ) for electrons and  
5 photons. For protons, where the data was provided, we used the 10% point of the distal edge  
6 enclosing the Bragg peak at energy using the dose depth curves from Kang for the energy 28-  
7 227 MeV [ 75]. As those data were taken with water, we scaled to range data for tissue by Usta  
8 averaging over eight tissue types [ 76].

9 The x-ray pinhole camera for FXR was designed and built for measuring the x-ray spot size  
10 as a function of time. It consisted of a “pinhole” composed of a series of tungsten cylinders  
11 stacked in a 15 cm long stainless-steel holder. Each cylinder had a hole formed by EDM, ranging  
12 in diameter from 200 to 760  $\mu\text{m}$ . The cylinders were stacked to approximate a double-tapered  
13 cone, with a section of 200  $\mu\text{m}$  pinholes by 4 cm long in the center. Behind the single pinhole,  
14 the camera had four gated channels that record the x-ray images to CCD cameras. Each of the  
15 channels had a scintillator array to convert the x-rays to visible light, a mirror and relay lens to  
16 image the scintillator onto the input of a microchannel image intensifier, and a CCD camera fiber-  
17 optically coupled to the output of the intensifier. The unit was shielded from external radiation  
18 using W powder packed between aluminum plates. Each camera had a frame buffer that stores  
19 the image for readout after each shot. The cameras had standard analog video output, but it was  
20 transmitted to the FXR control room via a 4-channel fiber-optic link. Arming of the camera frame  
21 buffers was also done through this fiber optic link. The video was digitized by a Scion frame-

1 grabber and computer. NIH Image J was used for local analysis of the images. Calibration was  
2 done with geometric considerations and cross correlating the results with other spot size  
3 measuring techniques such as observing the blur over an opaque edge.

4 Simplified dose rate distributions were developed using experimental PDD curves at the  
5 proper energy. This approach takes the dose build up zone into account as well as the  
6 bremsstrahlung spectrum. The calculations were done in 2D using standard ray tracing  
7 techniques to each  $\approx$ cm sized voxel. The array was then processed to provide the dose map. In  
8 addition, we used numerical approximations to crosscheck our results. Namely we use:  $I_T =$   
9  $\sum_{i=1}^N I_i$ , where  $I_T$  is the total dose rate and  $I_i$  is each source rate  $i$ . In the dose fall off region, we  
10 estimate the dose rate as a function of depth using an exponential function; the PDD curves  
11 correlated well to this function, with  $\chi^2 = 0.9997$ .

12 The key requirements for managing radiation induced toxicity is to maintain  $>40 \text{ Gy}\cdot\text{s}^{-1}$   
13 or preferably  $>100 \text{ Gy}\cdot\text{s}^{-1}$ . While it is not completely clear what the instantaneous dose rate  
14 should be, some suggest  $\approx 10^6 \text{ Gy}\cdot\text{s}^{-1}$  [ 6]. Our goal is high gradient requiring that the pulse width  
15 of the LIA be kept as short as possible but is limited by magnetic core response. Typical  
16 response is as fast as 6-8 ns [ 77]. This result allows a practical minimum pulse width of  
17 approximately 15 ns. As stated earlier, our calculation is based on electrons to bremsstrahlung  
18 instantaneous dose rate scaling as:  $1.7 \times 10^4 IV^{2.65}$ , where  $V$  is in MV and beam current  $I$ , is in  
19 kA and is a relatively good predictor for dose rate in  $\text{Gy}\cdot\text{s}^{-1}$  for Ta at 1 m distance. Instantaneous  
20 dose rate is thus defined by the current and electron energy and average dose rate is  
21 determined by the pulse repetition rate and pulse width.

## 1 References

1. Feder, T., High radiation dose rates may improve cancer therapy. *Physics today* **73** (12), 24-26 (2020).
2. Vozenin, M.-C. *et al.*, The Advantage of FLASH Radiotherapy Confirmed in Mini-pig and Cat-cancer Patients. *Clin Cancer Res* **25** (1), 35-42 (2019).
3. Schuler, E. *et al.*, Experimental Platform for Ultra-high Dose Rate FLASH Irradiation of Small Animals Using a Clinical Linear Accelerator. *Int J of Rad Oncology Biol Phys* **97** (1), 195-203 (2017).
4. Montay-Gruel, P. *et al.*, Irradiation in a flash: Unique sparing of memory in mice after whole brain irradiation with dose rates above 100 Gy/s. *Radiotherapy and Oncology* **124** (3), 365-369 (2017).
5. Zlobinskaya, O. *et al.*, The Effects of Ultra-High Dose Rate Proton Irradiation on Growth Delay in the Treatment of Human Tumor Xenografts in Nude Mice. *Radiat. Res.* **181** (2), 177-183 (2014).
6. Wilson, J. D., Hammond, E. M., Higgins, G. S. & Petersson, K., Ultra-High Dose Rate (FLASH) Radiotherapy: Silver Bullet or Fool's Gold? *Front. Oncology* **9**, 1563 (2020).
7. Esplen, N., Mendonca, M. S. & Bazalova-Carter, M., Physics and biology of ultrahigh dose-rate (FLASH) radiotherapy: a topical review. *Phys. Med. Biol.* **65** (23), 1-37 (2020).
8. Bourhis, J. *et al.*, Treatment of a first patient with FLASH-radiotherapy. *Radiotherapy and Oncology* **139**, 18-22 (2019).
9. Jaccard, *et al.*, High dose-per-pulse electron beam dosimetry: Commissioning of the Oriatron eRT6 prototype linear accelerator for preclinical use. *Med. phys.* **45** (2), 863–874 (2018).
10. Mole, R. H., The LD50 for uniform low LET irradiation of man. *British J. Radiology* **57** (677), 355-369 (1984).
11. Berry, R. J., Hall, E. J., Forster, D. W., Storr, T. H. & Goodman, M. J., Survival of mammalian cells exposed to X rays at ultra-high dose-rates. *British J. Radiology* **42** (494), 102-107 (1969).
12. Maxim, P. G., Keall, P. & Cai, J., Point/Counterpoint, FLASH radiotherapy: Newsflash or flash in the pan? *Med. Phys.* **46** (10), 4287-4290 (2019).
13. Favaudon, V. *et al.*, Ultrahigh dose-rate FLASH irradiation increases the differential response between normal and tumor tissue in mice. *Sci. Transl. Med.* **6** (245), 245ra93 (2014).
14. Karsch, L. *et al.*, Dose rate dependence for different dosimeters and detectors: TLD, OSL, EBT films, and diamond detectors. *Med. Phys.* **39** (5), 2447-2455 (2012).
15. Lempart, M. *et al.*, Modifying a clinical linear accelerator for delivery of ultra-high dose rate irradiation. *Radiotherapy Oncology* **139**, 40-45 (2019).

16. Crosbie, J. C. *et al.*, Energy spectra considerations for synchrotron radiotherapy trials on the ID17 bio-medical beamline at the European Synchrotron Radiation Facility. *J. Synchrotron Rad.* **22**, 1035–1041 (2015).
17. Archer, J. *et al.*, High spatial resolution scintillator dosimetry of synchrotron microbeams. *Sci. Rep.* **9**, 6873 (2019).
18. Bazalova-Carter, M. & Esplen, N., On the capabilities of conventional x-ray tubes to deliver ultra-high (FLASH). *Med. Phys.* **46** (12), 5690-5695 (2019).
19. Van de Walle, J. *et al.*, *The SCC@: from source to extraction*, presented at Proceedings of Cyclotrons 2016, Zurich, Switzerland, 2016 (unpublished).
20. Henrotin, S. *et al.*, *Commissioning and testing of the first IBA S2C2*, presented at Proceedings of Cyclotrons 2016, Zurich, Switzerland, 2016 (unpublished).
21. Zwart, T. *et al.*, *Developing a modern, high-quality proton therapy medical device with a compact superconducting synchrocyclotron*, presented at Centro de Investigaciones Energeticas, Medioambientales y Tecnologicas (CIEMT) 2016, Madrid, Spain, 2016 (unpublished).
22. Darafsheh, A. *et al.*, Feasibility of proton FLASH irradiation using a synchrocyclotron for preclinical studies. *Med. Phy. Lett.* **47** (9), 4348-4355 (2020).
23. Girdhani, S. *et al.*, *FLASH: A novel paradigm changing tumor irradiation platform that enhances therapeutic ratio by reducing normal tissue toxicity and activating immune pathways*, presented at American Association for Cancer Research Annual Meeting 2019, Atlanta, GA USA, 2019 (unpublished).
24. Dollinger, G. *et al.*, Nanosecond pulsed proton microbeam. *Nucl. Instr. Meth. Phys. Res. B* **267**, 2008–2012 (2009).
25. Smyth, L. M. L. *et al.*, Comparative toxicity of synchrotron and conventional radiation therapy based on total and partial body irradiation in a murine model. *Sci. Rep.* **8**, 12044 (2018).
26. van Marlen, P. *et al.*, Bringing FLASH to the clinic: Treatment planning considerations for ultrahigh dose-rate proton beams. *Int. J. Radiation Oncol. Biol. Phys.* **106** (3), 621-629 (2020).
27. Mohan, R. & Grosshans, D., Proton therapy – Present and future. *Adv. Drug Del. Rev.* **109**, 26–44 (2017).
28. Holmes, T. & Mackie, T. R., A filtered backprojection dose calculation method for inverse treatment planning. *Med. Phys.* **21** (2), 303-313 (1994).
29. Flynn, R. T., Barbee, D. L., Mackie, T. R. & Jeraj, R., Comparison of intensity modulated x-ray therapy and intensity modulated proton therapy for selective subvolume boosting: a phantom study. *Phys. Med. Biol.* **52**, 6073-6090 (2007).

30. Maxim, P. G., Tantawi, S. G. & Loo, B. W., PHASER: A platform for clinical translation of FLASH cancer radiotherapy. *Radiotherapy and Oncology* **139**, 28-33 (2019).
31. Ginzton, E. L., Hansen, W. W. & Kennedy, W. R., A linear electron accelerator. *Rev. Sci. Instr.* **19**, 89-108 (1948).
32. Neal, R. B., Design of linear electron accelerators with beam loading. *J. Appl. Phys.* **26** (7), 1019-1024 (1958).
33. Khizhnyak, N. A., Tolok, V. T., Checkkin, V. V. & Nazarov, N. I., The acceleration of large current pulses in electron linear accelerators. *Plasma Physics (J. Nucl. Ener. C)* **4**, 129-134 (1962).
34. Uetomi, I., Yamazaki, M., Kobayashi, H. & Sato, I., Extended Theory of Beam Loading in Electron Linac. *Jpn. J. Appl. Phys.* **32** (6A), 2858-2864 (1993).
35. Panofsky, W. K. H. & Bander, M., Asymptotic theory of beam break-up in linear accelerators. *Re. Sci. Instr.* **39** (2), 206-212 (1968).
36. Humphries, S., *Charged Particle Beams* (John Wiley and Sons, Hoboken, NJ, 1990).
37. Christofilos, N. C. *et al.*, High current linear induction accelerator for electrons. *Rev. Sci. Instr.* **35** (7), 886-890 (1964).
38. Takayama, K. & Briggs, R. J., *Induction Accelerators* (Springer, New York, 2011).
39. Seidl, *et al.*, Irradiation of materials with short, intense ion pulses at NDCX-II. *Laser and Part. Beams* **35** (2), 373-378 (2017).
40. Waldron, W. L. *et al.*, The NDCX-II engineering design. *Nucl. Instr. Meth. Phys. Res. A* **733**, 226-232 (2014).
41. Barnard, J. J. *et al.*, Induction accelerator architectures for heavy-ion fusion. *Nucl. Instr. Meth. in Phys. Res. A* **415** (1-2), 218-228 (1998).
42. Smith, J. R., Bailey, V. L., Lackner, H. & Putnam, S. D., *Performance of the spiral line induction accelerator*, presented at Proceedings of the 1997 Particle Accelerator Conference, Vancouver, BC Canada, 1997 (unpublished).
43. Beal, J. W., Christofilos, N. C. & Hester, R. E., The Astron Linear Accelerator. *IEEE Trans. Nucl. Sci.* **16** (3), 294-298 (1969).
44. Allen, S. L. *et al.*, *Generation of high power 140 GHz microwaves with an FEL for the MTX experiment*, presented at Proceedings of International Conference on Particle Accelerators, Washington, DC USA, 1993 (unpublished).

45. Yatsui, K. *et al.*, *Pulse-power technology and its applications at LBT, Nagaoka*, presented at 11th International Conference on High-Power Particle Beams, Prague, Czech Republic, 1996 (unpublished).
46. Anthouard, P. *et al.*, *Airix at CESTA*, presented at 11th International Conference on High-Power Particle Beams, Prague, Czech Republic, 1996 (unpublished).
47. Fateev, A. A. *et al.*, *Status of the first stage of linear induction accelerator SILUND-21*, presented at Proceedings Particle Accelerator Conference, Dallas, TX USA, 1995 (unpublished).
48. Deng, J. *et al.*, *Upgrading of Linear Induction Accelerator X-Ray Facility (LIAXF)*, presented at 19th International Linear Accelerator Conference, Chicago, IL USA, 1998 (unpublished).
49. Kulke, B. & Kihara, R., Recent Performance Improvements on FXR. *IEEE Trans. Nucl. Sci.* **30** (4), 3030-3032 (1983).
50. Burns, M. J. *et al.*, *Status of the DARHT phase 2 long-pulse accelerator*, presented at 2001 Particle Accelerator Conference, Chicago, IL USA, 2001 (unpublished).
51. Burns, M. J. *et al.*, *DAHRT accelerators update and plans for initial operation*, presented at Particle Accelerator Conference, New York, NY USA, 1999 (unpublished).
52. Merle, E. *et al.*, *Installation of the AIRIX Induction Accelerator*, presented at 19th International Linear Accelerator Conference, Chicago, IL USA, 1998 (unpublished).
53. Deng, J. *et al.*, *Design of the DRAGON-I Linear Induction Accelerator*, presented at 21st International Linear Accelerator Conference, Gyeongju, Korea, 2002 (unpublished).
54. Reginato, L., The Advanced Test Accelerator (ATA), a 50-MeV 10-kA Induction Linac. *IEEE Trans. Nucl. Sci.* **30**, 2970-2974 (1983).
55. Multhauf, L. G., Back, N. L., Simmons, L. F., Zentler, J.-M. & Scarpetti, R. D., *Invited: The LLNL flash x-ray induction linear accelerator (FXR)*, presented at Proc. SPIE 4948, 25th International Congress on High-Speed Photography and Photonics, Beaune, France, 2003 (unpublished).
56. Darwin, D.-M. H., 1999.
57. Negre, J. P. & Rubbelynck, C., Application of fast CVD diamond photoconductor detectors to MeV X-ray metrology for the AIRIX fash radiographic facility. *Nucl. Instr. Meth. Phys. Res.* **A 451**, 638-650 (2000).
58. Thumm, M., State-of-the-Art of High-Power Gyro-Devices and Free Electron Masers. *J. Infrared Milli Terahz Waves* **41**, 1–140 (2020).

59. Sampayan, S. *et al.*, *Performance characteristics of an induction linac magnetic pulse compression modulator at multi-kilohertz pulse repetition frequencies*, presented at IEEE Particle Accelerator Conference, San Francisco, CA USA, 1991 (unpublished).
60. Sampayan, S. E. *et al.*, Characterization of carrier behavior in photonically excited 6H silicon carbide exhibiting fast, high voltage, bulk transconductance properties. *Sci. Rep.* **11**, 6859 (2021).
61. Sampayan, S. E., US Patent No. 10,270,368 (April 2019).
62. Narayanasamy, G. *et al.*, Commissioning an Elekta Versa HD linear accelerator. *J. Appl. Clinical Med. Phys.* **17** (1), 179-191 (2016).
63. Feye, A. T., Percentage depth dose and beam profile measurements for electron and photon beam in reference field size for different energies. *Intl. J. Sci. Engr. Res.* **9** (2), 1460-1464 (2018).
64. Fryar, C. D., Kruszon-Moran, D., Gu, Q. & Ogden, C. L., 2018.
65. Schulz, J. W., Innovation in X-Ray technology. *Revista Matéria* **16** (4), 867-876 (2011).
66. Dalakos, G. T., Frontera, M. A. & Robinson, V. S., United States Patent No. 9,715,989 B2 (July 2017).
67. Humphries, S., *Principals of Charged Particle Acceleration* (John Wiley and Sons, Hoboken, NJ, 1999).
68. Sampayan, S. E., Vitello, P. A., Krogh, M. L. & Elizondo, J. M., Multilayer high gradient insulator technology. *IEEE Trans. Dielect. Elect. Insul.* **7** (3), 334-339 (2000).
69. Sampayan, S. E., Caporaso, G. J., Houck, T. L. & Watson, J. A., Multilayer high gradient insulator testing in the vicinity of charged particle beams. (*to be published*).
70. Harris, J. R., Kendig, M., Poole, B., Sanders, D. M. & Caporaso, G. J., Electrical strength of multilayer insulators. *Appl. Phys. Lett* **93**, 241502 (2008).
71. Shang, C. C. *et al.*, *BBU design of linear induction accelerator cells for radiography application*, presented at 1997 Particle Accelerator Conference, Vancouver, BC Canada, 1997 (unpublished).
72. El-Ghossain, M. O., Calculations of stopping power, and range of ions radiation (alpha particles) interaction with different materials and human body parts. *Int. J. of Phys.* **5** (3), 92-98 (2017).
73. Hill, R. *et al.*, Advances in kilovoltage x-ray beam dosimetry. *Phys. Med. Biol.* **59** (6), 183-231 (2014).
74. Turner, J. E., *Atoms, Radiation, and Radiation Protection* (Wiley, Inc., Hoboken, NJ, USA, 2008).
75. Kang, M., Cessac, R. & Pang, D., Commissioning and beam characterization of the first gantry-mounted accelerator pencil beam scanning proton system. *Med. Phys.* **47**, 3496-3510 (2020).

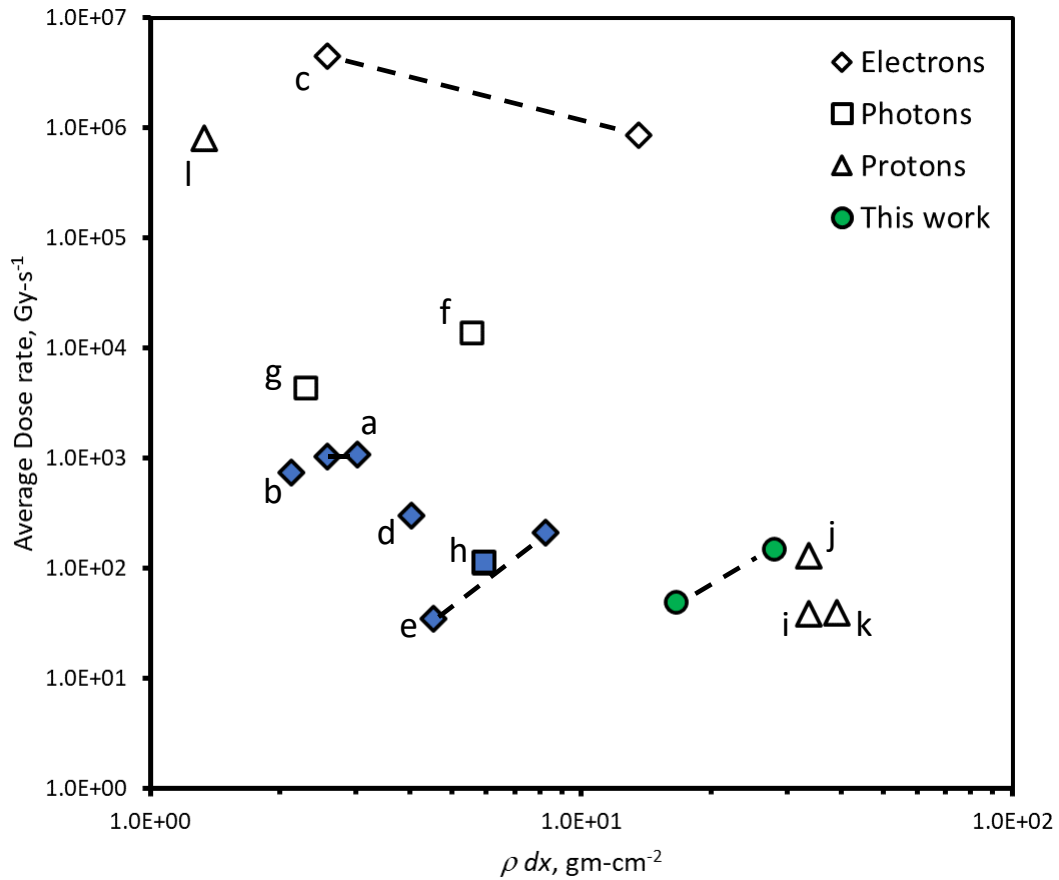
76. Usta, M. & Tufan, M. Ç., Stopping power and range calculations in human tissues by using the Hartree-Fock-Roothaan wave functions. *Rad. Phys. Chem.* **140**, 43-50 (2017).
77. Corcoran, P. *et al.*, *Experimental tests of the power supply and prototype cell for the 1.5 MeV SLIA acceleration unit*, presented at 1991 IEEE Particle Accelerator Conference, San Francisco, CA USA, 1991 (unpublished).



1

2 Figure 1 – Effects of 167 GY/s (15-Gy in 90-ms) electron beam treatment of a 3.5-cm skin tumor  
3 in the first FLASH-RT of a human subject. Top: Day 0, middle: Day 21, bottom: ~Day 150 [ 8]  
4 (Reprinted with permission, License No. 5054930939964).

5

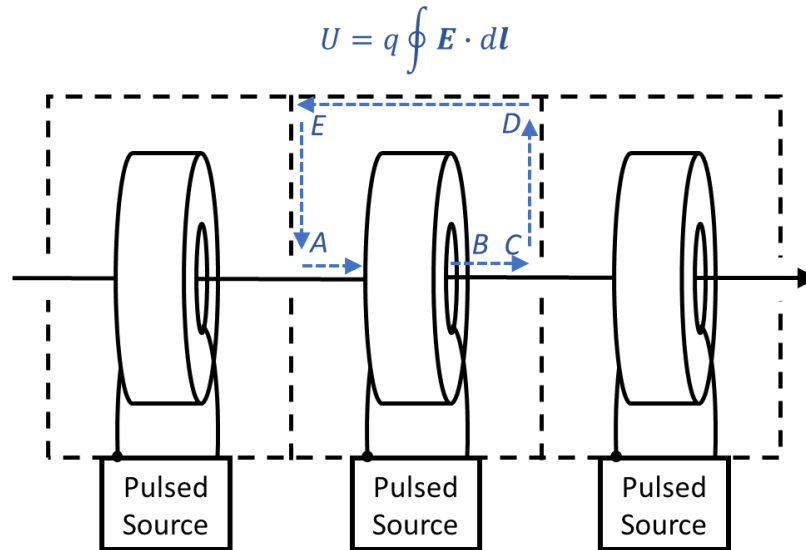


1

2 Figure 2 – A survey of FLASH-RT average dose rate as a function of range calculated from details  
 3 obtained from the literature. See Table I for specific details. Solid blue markers designate clinic  
 4 scale systems that can be placed in approximately a 100 m<sup>3</sup> radiation vault. Dotted line signifies  
 5 the approximate range of a particular single system.

6

1



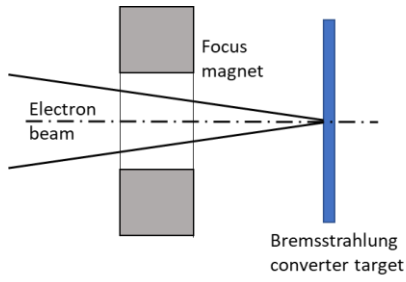
2

3 Figure 3 – Acceleration of charged particles (on axis arrow) with a linear induction accelerator  
 4 (LIA). Here  $U$  is the energy gain,  $q$  is the particle charge, and  $\mathbf{E}$  is the electric field. Magnetic  
 5 cores are depicted by the toroids and the dotted lines indicate conductive surfaces. One side of  
 6 the pulsed source is referenced to the accelerator cavity interior (represented by the dot). The  
 7 electric field outside the structure is everywhere essentially zero within the diffusion time  
 8 scales of the conductive walls. Thus, the line integral is zero from segments C to A as the  
 9 electric field is shorted by the conducting wall. The contribution along AB is also zero as the  
 10 pulsed source output is referenced to the cavity wall. The only contribution is along line  
 11 segment BC, where charge particles gain energy during the pulse.  $N$  cavities are arranged in  
 12 series to provide a total acceleration of  $NV_{pulsed\ source}$ .

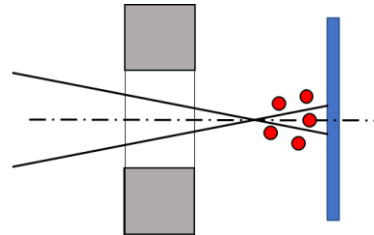
13

1

**a**

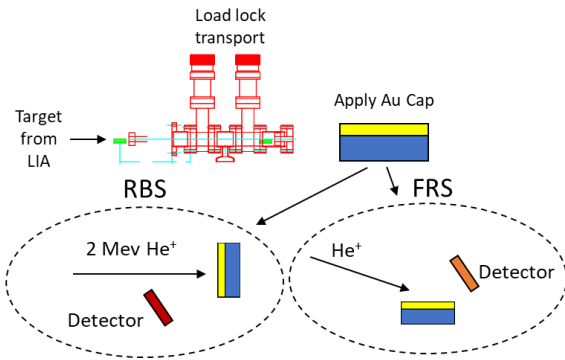


**b**

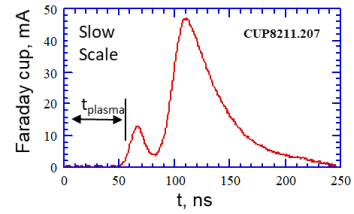
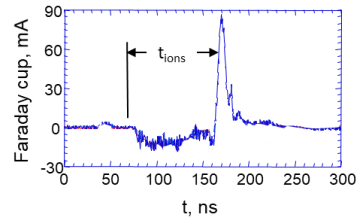


2

**c**

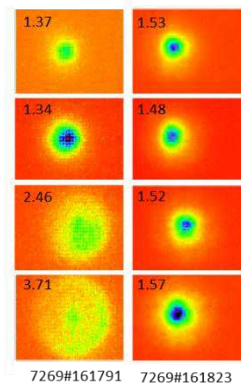


**d**

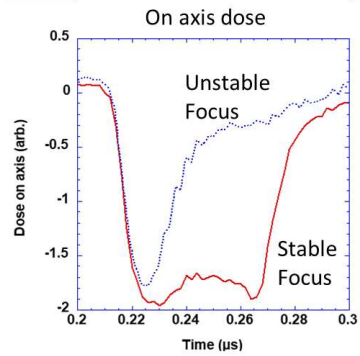


3

**e**

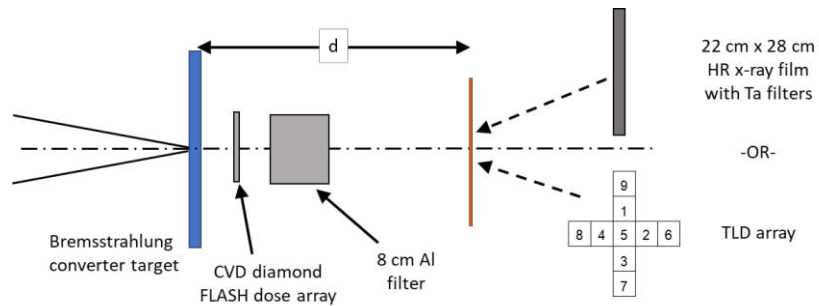


**f**



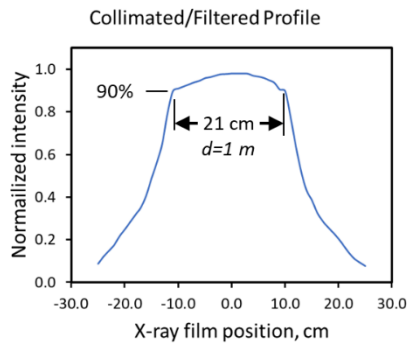
4

**g**

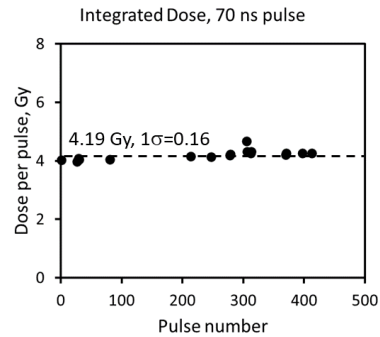


1

**h**



**i**



2

3 Figure 4 – Experiments stabilizing the bremsstrahlung pulse from the Flash X-ray (FXR) linear  
4 induction accelerator. (a), (b) Depict a primary mechanism of spoiling the beam focus in a pulse;  
5 ions created by the electron beam interaction create a plasma where the space charge of the  
6 beam accelerates ions away from the target and partially neutralizes the beam. (c) Depicts a  
7 method used to determine the surface and target contamination using Rutherford scattering  
8 and secondary ion mass spectroscopy. (d) Plasma measurements were made to determine the  
9 plasma expansion speed of both contaminants and target material. (e) Shows the dynamic  
10 bremsstrahlung spot behavior unmitigated (left) and mitigated (right) using measured focusing  
11 techniques. (f) Shows the impact of mitigating and not-mitigating back streaming plasma/ion  
12 from the target. (g)-(i) Shows the measurement geometry to determine bremsstrahlung field  
13 flatness and pulse-to-pulse repeatability.

14

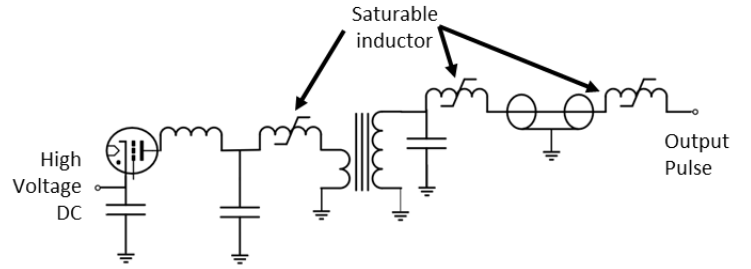
15

1

a

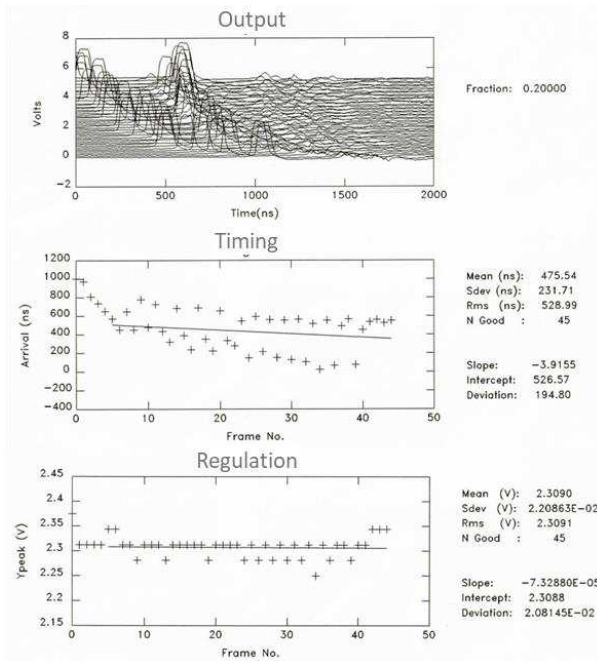


b

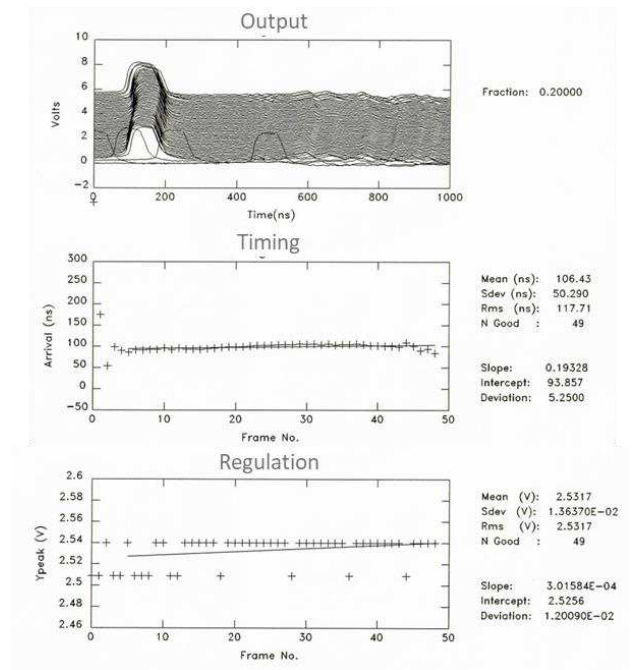


2

c



d



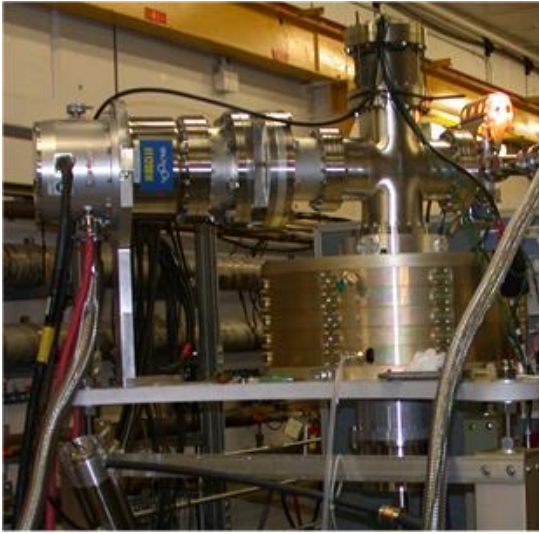
4

5

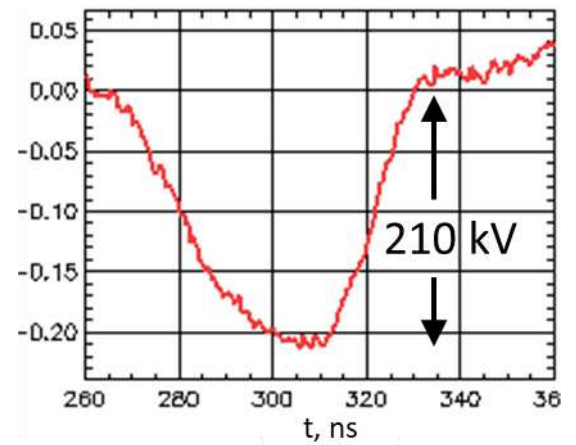
6

1

e

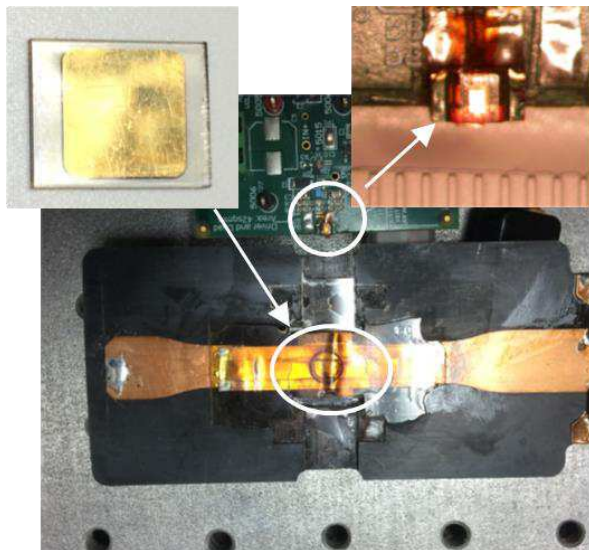


f

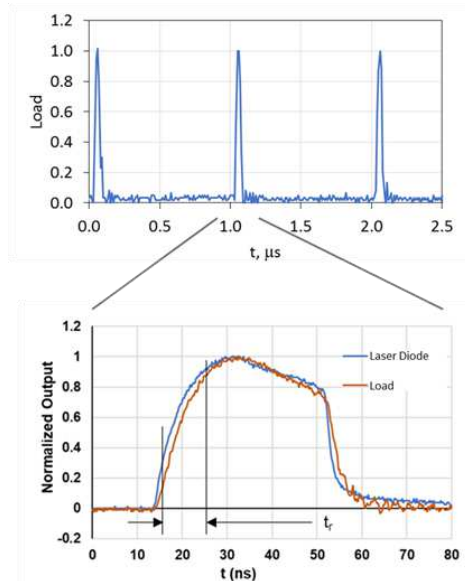


2

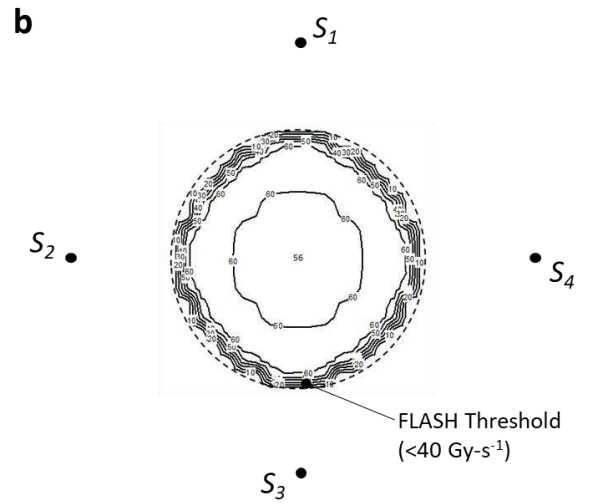
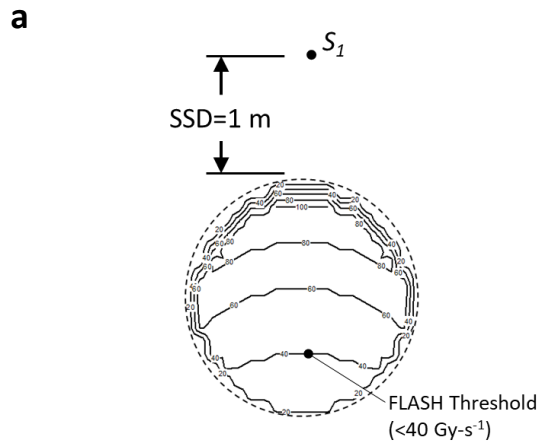
g



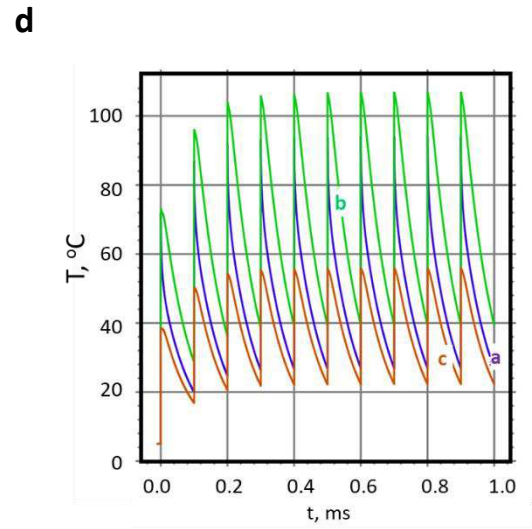
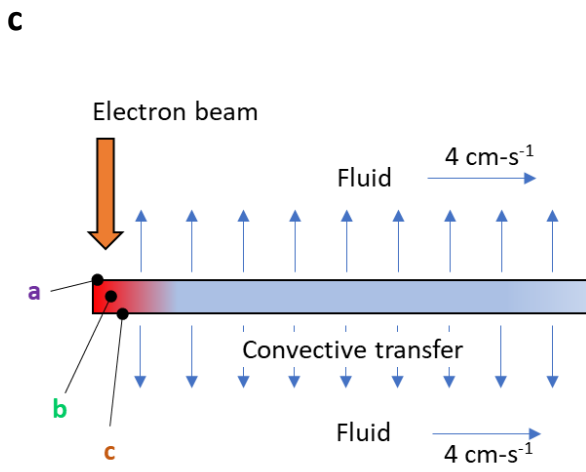
h



4 Figure 5 – Development of high repetition rate LIAs. (a) The Experimental Test Accelerator-II  
 5 (ETA-II) at Lawrence Livermore National Laboratory nominally rated at 3000-A beam current,  
 6 6.5 MeV, at 5 kHz (top) and the pulsed sources using thyatron gas switches and a Melville  
 7 pulse compression transmission line (bottom). (b) Schematic of the pulsed source. (c) (d) Effect  
 8 of stabilizing the repeatability of the pulsed sources at 5000 Hz. (e) (f) First tests on high  
 9 gradient cavities operating at 42 kV per cell using SF<sub>6</sub> insulation gas; we anticipate better than  
 10 twice the performance using oil insulation. (g) (h) Testing silicon carbide switching using the  
 11 optical transconductance varistor (OTV) technology 60.

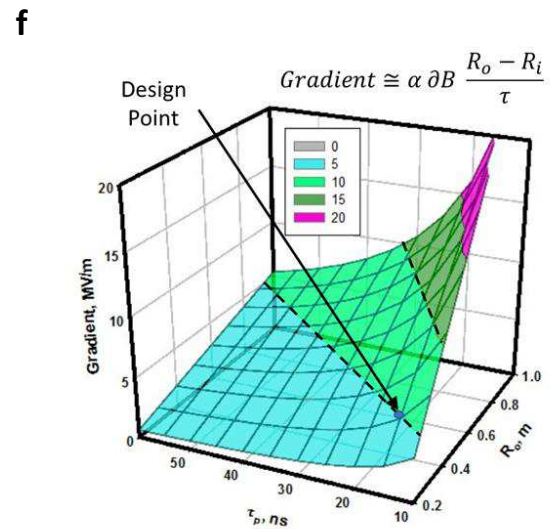
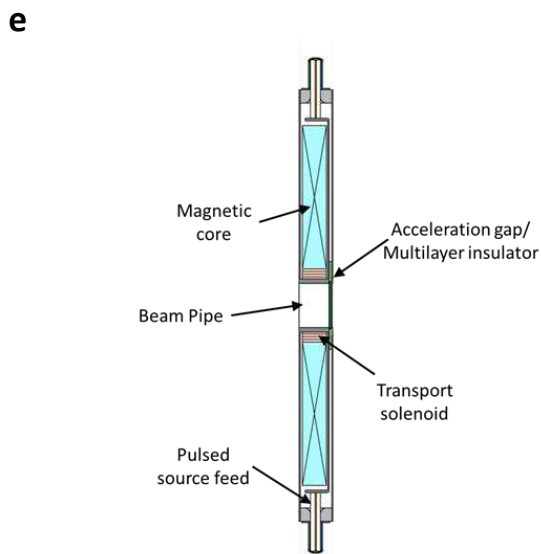


1

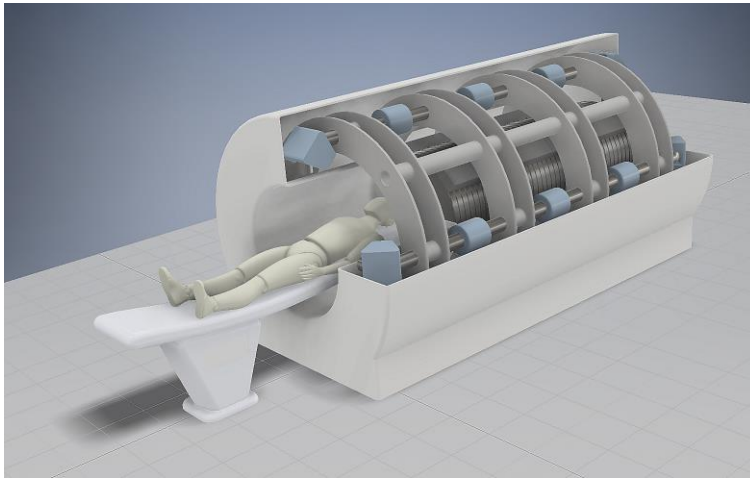


2

3



**g**



Parameter	Induction Linear Accelerator
Electron Energy (MeV)	16
Total Beam Current (A)	25
Pulse Width (s)	1.50E-08
Pulse Repetition Frequency (Hz)	10000
Net Gradient (MeV/m)	5.0
Accelerator Length (m)	3.20
Inner Radius (cm)	10.0
Instantaneous Surface Dose Rate (Gy/s)	6.60E+05
Average Surface Dose Rate (Gy/s)	98.9
Total Dose (Gy)	19.8
Time On (s)	0.20

1 Figure 6 – Point design considerations for a high gradient linear induction accelerator for  
 2 FLASH-RT. (a) (b)  $100 \text{ Gy-s}^{-1}$  single sources and four  $25 \text{ Gy-s}^{-1}$  multisource dose rate calculations  
 3 to deliver above the tissue sparing threshold and reduced toxicity. Single source results in a  
 4 below tissue sparing dose at the exit edge whereas the four sources provide a nearly uniform  
 5 distribution above the  $40 \text{ Gy-s}^{-1}$  healthy tissue sparing threshold. (c) (d) Cooled multilayer target  
 6 considerations. Multilayer target enables rapid cooling from the target interior causing the  
 7 target temperature to equilibrate at approximately  $110^\circ \text{ C}$ . (e) (f) Induction cavity design based  
 8 on volt-second properties of the core and the dimensions, where:  $\alpha$  - cavity packing efficiency,  
 9  $\partial B$  – flux swing of the magnetic core,  $R_i$  – core inner radius,  $R_o$  – core outer radius, and  $\tau$  –  
 10 accelerator pulse width. For our design point, we take  $R_i = 0.1\text{-m}$ ,  $\partial B \approx 0.6\text{T}$  (NiZn ferrite), and  $\alpha$   
 11 = 60% 67 38. (g) Concept FLASH RT system using a linear induction accelerator (LIA) providing  
 12 four lines-of-sight. LIA is on axis with the patient. Blue elements are magnetic focusing  
 13 elements that direct the electron beam to the patient. Accelerator is 3.2 m, overall system  
 14 length is 3.5 m less the patient couch.

15

16

1

2

TABLE I – Present methods of FLASH-RT delivery

Desig.	System	Technology		Energy, MeV	Average Dose Rate, Gy-s <sup>-1</sup>	Nominal Area, cm <sup>2</sup>	Reference
		Type System	Scale				
Electrons							
a	Oriatron (eRT6)	RF Linac	Clinical	4.9–6	1030-1080	55.0	Jaccard 2018
b	Kinetron	RF Linac	Clinical	4–5	750	3.10	Favaudon 2014
c	ELBec	Superconducting RF Linac	Large laboratory - Helmholtz-Zentrum Dresden-Rossendorf	5–40	0.86-4.5 x 10 <sup>6</sup>	0.79	Karsch 2012
d	Elekta Precise	RF Linac	Clinical	≈8	300	19.6	Lempart 2019
e	Varian Clinac 21EX	RF Linac	Clinical	9, 20	35-210	12.6	Schüler 2017
Photons							
f	ESRF (ID17)	Synchrotron	Large laboratory - European Synchrotron Radiation Facility	0.105	14000	0.50	Crosbie 2015
g	IMBL	Synchrotron	Large laboratory - Imaging and Medical Beam-Line, Australian Synchrotron	0.94	4441	0.60	Archer 2019
h	MXR 160/22	X-ray tube	Clinical	0.16	114	0.79	Bazalova-Carter 2019, Esplen 2019
Protons							
i	Proteus IBA	Superconducting synchro-cyclotron	Specialized clinic	230	39.1	0.79	Henrotin 2016, de Walle 2016
j	HyperScan Mevion	Superconducting synchro-cyclotron	Specialized clinic	230	130	1.10	Zwart 2016 Darafsheh 2020
k	ProBeam Varian (Based on publications)	Superconducting isochronous cyclotron	Specialized clinic	250	40.0	3.00	Abel 2019, Girdhani 2020, Darafsheh 2020
l	SNAKE Experimental (micro-beam)	Tandem Van de Graaff accelerator using a beam buncher	Large Laboratory - Maier-Leibnitz-Laboratorium	20	8.0 x 10 <sup>5</sup>	7.5 x 10 <sup>-5</sup>	Dollinger 2009

3

1  
2

TABLE II – Worldwide Linear Induction Accelerators (LIA) over 5 MeV.

Facility	Location	Energy (MeV)	Beam Current (A)	Pulse Width (ns)	Maxmium pulse repetition rate (Hz) [Total No. Pulses]	Reference
SLIA	Pulse Science Incorporated, USA	5.5	10,000	30		Smith, 1997
Astron	Lawrence Livermore National Laboratory, USA	6	800	300	1400 [100]	Beal, 1969
ETA-II	Lawrence Livermore National Laboratory, USA	6.5	3,000	50	5000 [50]	Allen, 1993
ETIGO-III	Nagaoka University, Japan	8	5,000	30	1	Yatsui, 1996
PIVAR	Centre d'études scientifiques et techniques d'Aquitaine-Cesta, France	8	3,500	80	1	Anthouard, 1996
SILUND-21	Joint Institute for Nuclear Research-Dubna, Russia	10	1,000	60		Fateev, 1995
LIAXF/LIAXFU	Institute of Fluid Physics, China	12	2,600	90	1	Deng, 1998
FXR	Lawrence Livermore National Laboratory, USA	17	3,000	60	0.3	Kulke, 1983
DARHT-II	Los Alamos National Laboratory, USA	17	2,100	1,600	1	Burns, 2001
DARHT-I	Los Alamos National Laboratory, USA	20	2,000	60	1	Burns, 1999
AIRIX	Centre d'études scientifiques et techniques d'Aquitaine-Pontfaverger-Moronvilliers, France	20	4,000	80	1	Merle, 1998
DRAGON-I	Institute of Fluid Physics, China	20	3,000	90	1	Deng, 2002
LIA 30/250	Joint Institute for Nuclear Research-Dubna, Russia	30	250	500	50	Takayama, 2011
ATA	Lawrence Livermore National Laboratory, USA	45	10,000	75	1000 [10]	Reginato, 1983

3  
4

1  
2  
3  
4  
5  
6  
7  
8  
9  
10  
11  
12  
13  
14  
15  
16  
17  
18  
19  
20  
21  
22  
23  
24  
25  
26  
27  
28  
29  
30  
31  
32  
33  
34  
35

**Supplementary Information**

**Acknowledgements** - This work was performed under the auspices of the U.S. Department of Energy by Lawrence Livermore National Laboratory under Contract DE-AC52-07NA27344. Work performed by Opcondys, Inc. was funded separately by the United States government under ARPA-E (Contract No. DE-AR0000907), the National Science Foundation (Grant No. 1519964), and the California Energy Commission CalSEED Program (Grant No. 17-01-03). We acknowledge Isik C. Kizilyalli, Eric Carlson, and Danny W. Cunningham for their guidance and encouragement of the high voltage switch work and especially the help of Ian D. Smith for his reading and key insights into the development of this manuscript. We especially wish to thank the FXR and ETA-II experimental staff, specifically Alan Hill and Blake Kreitzer.

**Author Contributions** - SES was the principal author and developed the overall approach for the system and conducted the initial bremsstrahlung target experiments. KCS conducted and led the photoconductive switch experiments, developed the thermal models for the high-power target, and analytical expression for the dose profile from multiple sources. GJC and YJC developed the LIA concepts and beam transport approaches. In addition, YCJ developed the optimized focusing approaches and led the physics theoretical work associated with the beam target interaction. SF developed and built the x-ray pinhole camera and took the gated images of the target spot behavior. SAH developed the concept along with the guidance of JH. In addition, JH provided the oncology expertise for the paper. JAW developed pulse and regulation stabilization algorithms and approaches for the 5 kHz pulsed sources. JMZ conducted the FXR stability experiments and FLASH detector calibrations.

**Competing Interests Statement** - This paper is a result of Federally sponsored research or development. The United States Government has rights to patents pursuant to Contract No. DE-AC52-07NA27344 between the United States Department of Energy and Lawrence Livermore National Security, LLC for the operation of Lawrence Livermore National Laboratory. Opcondys, Inc. is a for profit company and may profit from the technologies described in this paper.

**Disclaimer** - Reference herein to any specific commercial products, process, or service by trade name, trademark, manufacturer, or otherwise, does not necessarily constitute or imply its endorsement, recommendation, or favoring by the U.S. government or Lawrence Livermore National Security, LLC. The views and opinions of authors expressed herein do not necessarily state or reflect those of the U.S. government or Lawrence Livermore National Security, LLC, and shall not be used for advertising or product endorsement purposes.

## Figures



**Figure 1**

Effects of 167 GY/s (15-Gy in 90-ms) electron beam treatment of a 3.5-cm skin tumor in the first FLASH-RT of a human subject. Top: Day 0, middle: Day 21, bottom: ~Day 150 [ 8] (Reprinted with permission, License No. 5054930939964).

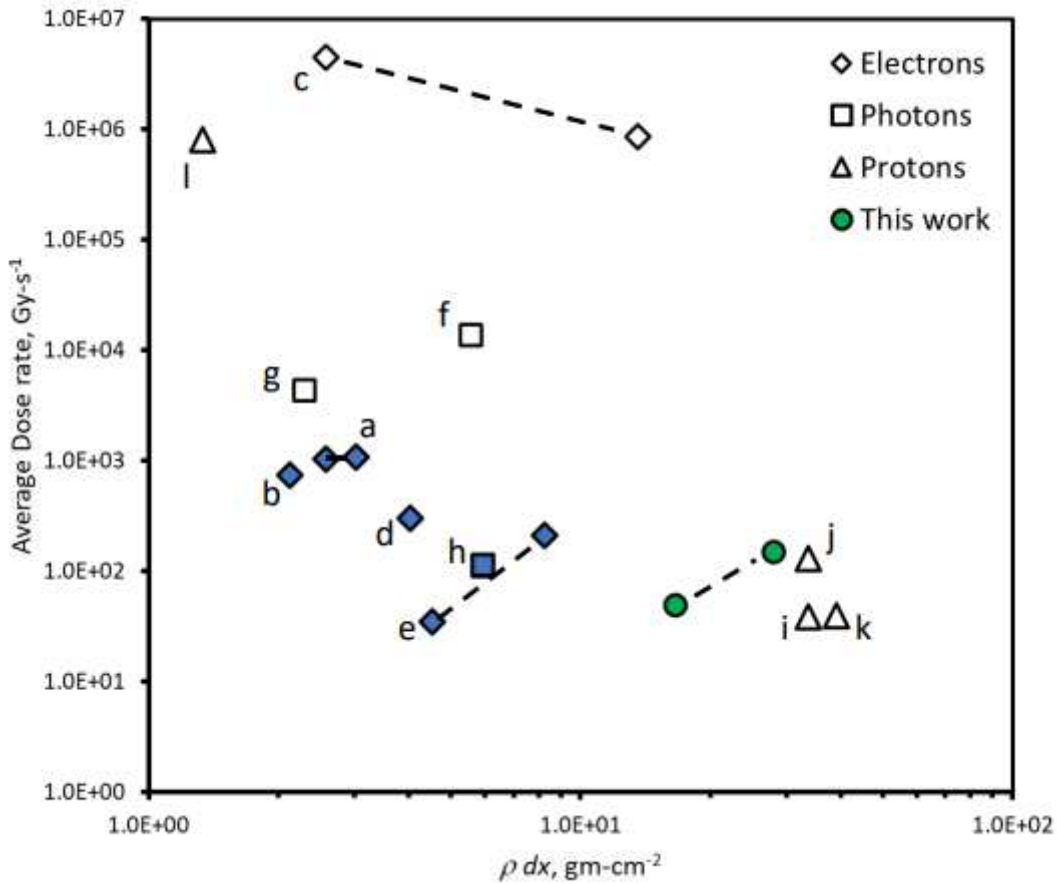


**Figure 2**

A survey of FLASH-RT average dose rate as a function of range calculated from details obtained from the literature. See Table I for specific details. Solid blue markers designate clinic scale systems that can be placed in approximately a 100 m<sup>3</sup> radiation vault. Dotted line signifies the approximate range of a particular single system.

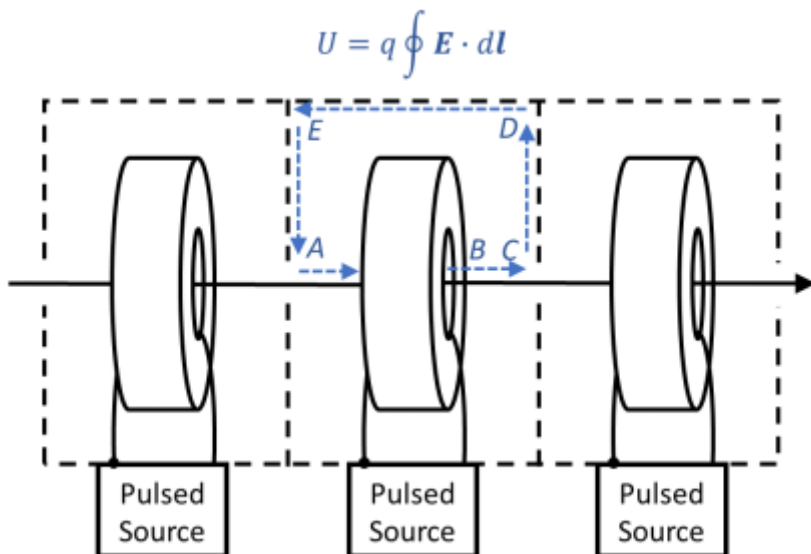


**Figure 3**

Acceleration of charged particles (on axis arrow) with a linear induction accelerator (LIA).

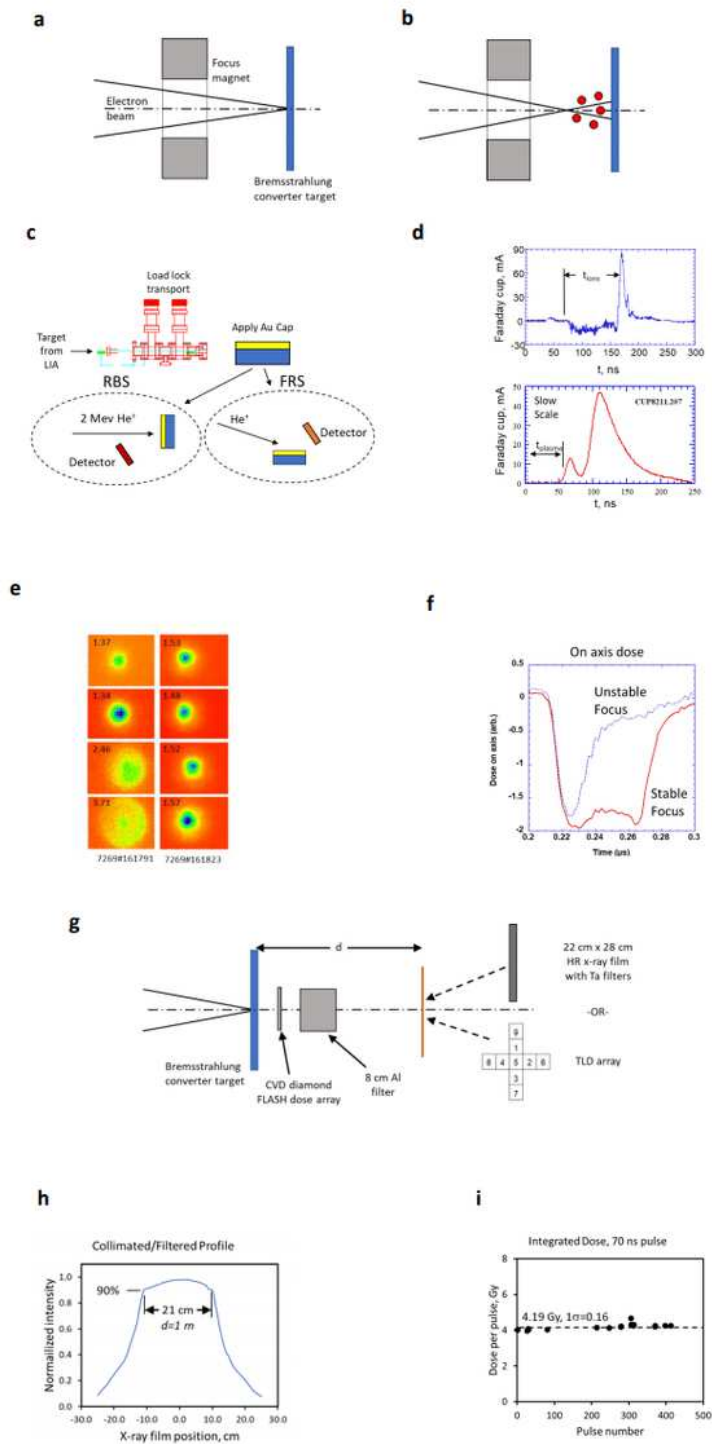


**Figure 4**

Experiments stabilizing the bremsstrahlung pulse from the Flash X-ray (FXR) linear induction accelerator.

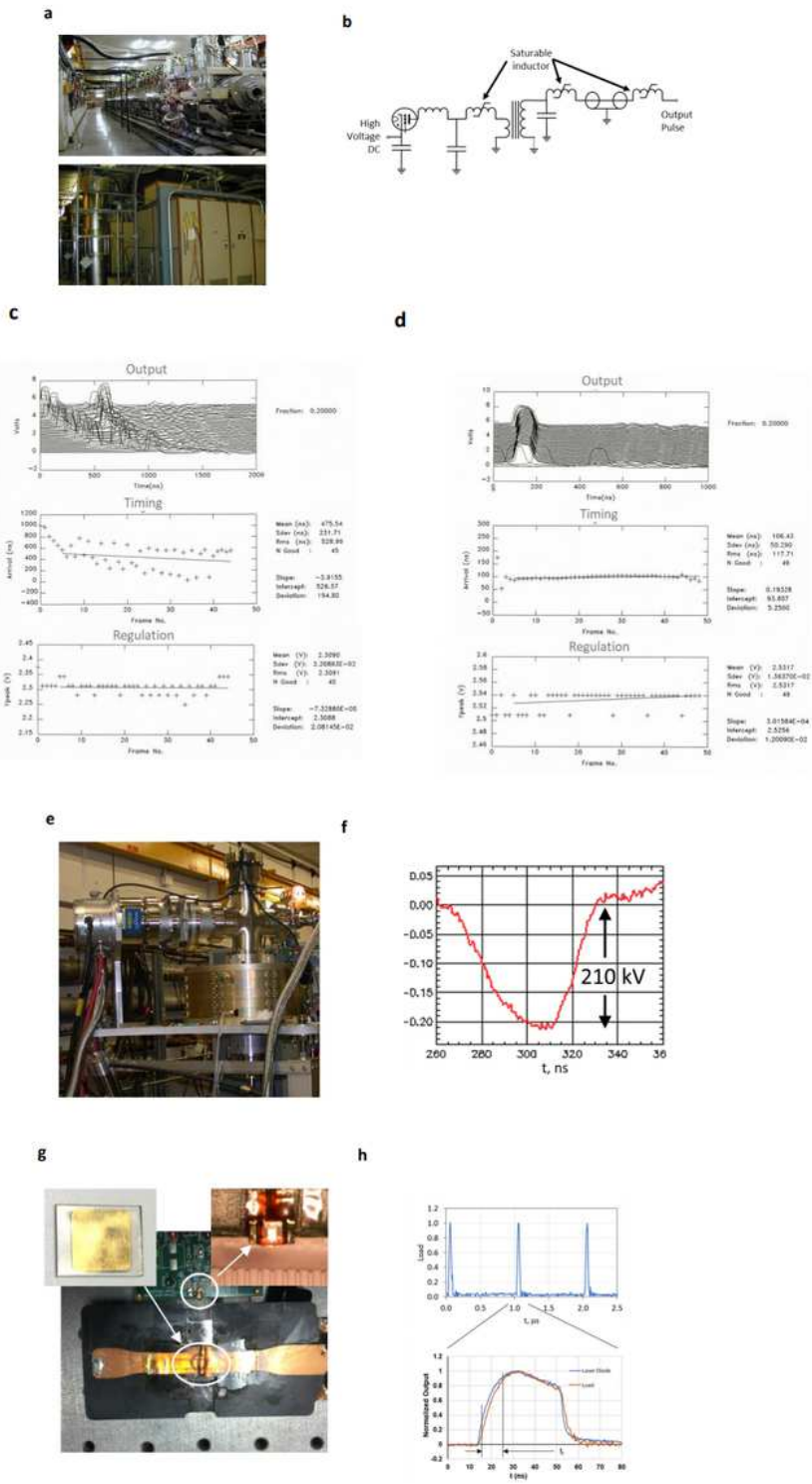


**Figure 5**

Development of high repetition rate LIAs.

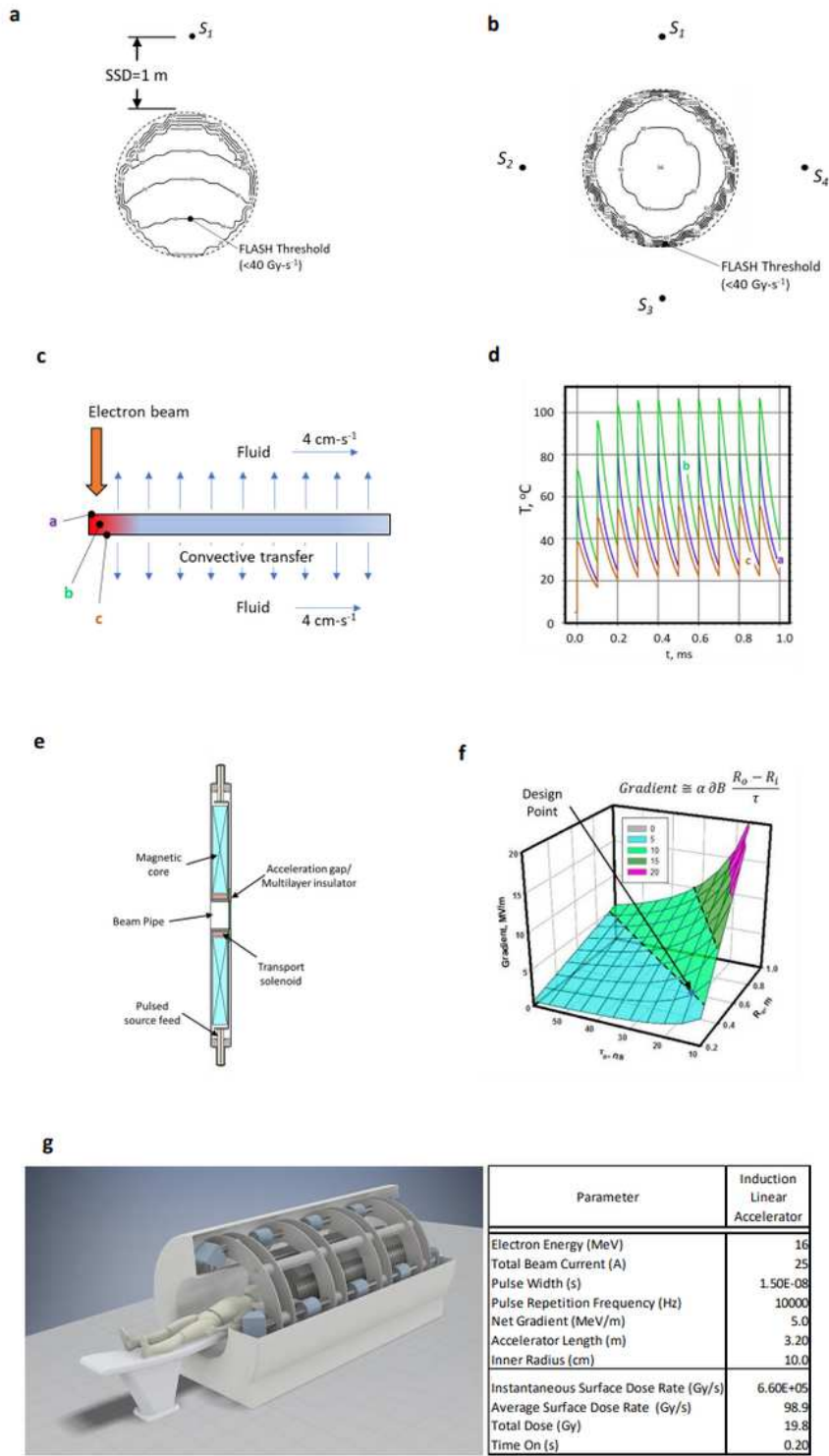


**Figure 6**

Point design considerations for a high gradient linear induction accelerator for FLASH-RT.